OPTICS

Precise multispecies agricultural gas flux determined using broadband open-path dual-comb spectroscopy

Daniel I. Herman[1,2]*, Chinthaka Weerasekara[3], Lindsay C. Hutcherson[4], Fabrizio R. Giorgetta[1,2], Kevin C. Cossel[1], Eleanor M. Waxman[1], Gabriel M. Colacion[1], Nathan R. Newbury[1], Stephen M. Welch[3], Brett D. DePaola[4], Ian Coddington[1], Eduardo A. Santos[3], Brian R. Washburn[5]

Advances in spectroscopy have the potential to improve our understanding of agricultural processes and associated trace gas emissions. We implement field-deployed, open-path dual-comb spectroscopy (DCS) for precise multispecies emissions estimation from livestock. With broad atmospheric dual-comb spectra, we interrogate upwind and downwind paths from pens containing approximately 300 head of cattle, providing time-resolved concentration enhancements and fluxes of CH_4, NH_3, CO_2, and H_2O. The methane fluxes determined from DCS data and fluxes obtained with a colocated closed-path cavity ring-down spectroscopy gas analyzer agree to within 6%. The NH_3 concentration retrievals have sensitivity of 10 parts per billion and yield corresponding NH3 fluxes with a statistical precision of 8% and low systematic uncertainty. Open-path DCS offers accurate multispecies agricultural gas flux quantification without external calibration and is easily extended to larger agricultural systems where point-sampling-based approaches are insufficient, presenting opportunities for field-scale biogeochemical studies and ecological monitoring.

INTRODUCTION

In the United States, methane (CH_4) emissions from livestock (including enteric fermentation and manure management) are thought to be the largest source of anthropogenic CH_4 emissions (*1*), with most of these emissions attributed to the beef and dairy industries. Precise estimation of livestock CH_4 emissions is challenging due to variability of management practices and cattle characteristics in commercial farms. Furthermore, in grazing systems, environmental drivers affect the forage quality (*2*), which, in turn, affects the enteric fermentation CH_4 emissions but remain unaccounted for in national inventories (*3*, *4*). Characterizing CH_4 flux from grazing systems is difficult as animals are unevenly distributed, limiting the efficacy of optical point sensor approaches (*5*). Cattle farms also emit considerable amounts of ammonia (NH_3), a harmful aerosol-generating pollutant (*6*). Quantification of NH_3 emissions using traditional methods is challenging due to its adsorptivity (*7*–*9*). Here, we show that the dual-comb spectroscopy (DCS) technique is capable of precisely measuring these important emissions without large systematic biases.

Open path DCS is emerging as a powerful tool for determining greenhouse gas (GHG) emissions in the urban (*10*) and oil/gas (*11*) sectors. In DCS, the interference of two optical frequency combs generates extremely high-resolution, broadband spectra, with negligible instrument lineshape and a perfect frequency axis, while requiring no external calibration (*12*–*14*). Together, these properties improve the analysis of overlapping spectral features that appear in broadband atmospheric spectra and allow DCS to provide accurate path-averaged multispecies concentrations and temperature measurements (*15*). In addition, the high brightness and spatial coherence of comb sources enable precise spectroscopic measurements over kilometer-scale paths. The precision achievable by DCS will lead to less uncertainty on livestock CH_4 emission rates, thus improving the overall uncertainty of national-level enteric fermentation models (*16*–*18*).

Here, we demonstrate DCS for multispecies (CH_4, NH_3, CO_2, and H_2O) quantification of gas emission flux from a small beef cattle feedlot and simultaneously validate the DCS system against a closed-path cavity ring-down spectroscopy (CRDS) gas analyzer. Measurements were performed between October 2019 to January 2020 and yielded over 10 days of CH_4 flux data for a field comparison of the two techniques. Fluxes are determined using an inverse Lagrangian dispersion model (IDM) that combines meteorological data with upwind and downwind concentrations from both the DCS and CRDS, and CH_4 fluxes from both systems agree to within model error. Our experimental design enables reliable benchmarking against a standard technique; however, the open-path DCS should allow for precise flux estimation in much larger pasture systems with sparser point sources. In addition, NH_3 emission rates from the feedlot are also determined using DCS with statistical precision of <10%, highlighting the versatility of broadband open-path laser spectroscopy for agricultural sensing.

Dual-comb system

The open-path DCS system (Fig. 1A) covers 35 THz from 1.4 to 1.7 μm with fully coherent frequency combs that can resolve the atmospheric transmission across over 175,000 individual comb teeth. The system is designed to target multiple gas species with laboratory-level precision while operating in the field conditions of a cattle feedlot (Fig. 1, B and C). It is based on all-polarization–maintaining, semiconductor saturable absorber mirror (SESAM)–modelocked erbium-doped fiber lasers with repetition rates near 200 MHz. Mutual comb coherence is established by phase locking each comb to the same free-running 1560-nm external-cavity diode laser and by phase locking the carrier-envelope offset frequency (f_0) of each comb using an in-line f-to-$2f$ interferometer (*19*). In addition,

[1]Applied Physics Division, National Institute of Standards and Technology, Boulder, CO 80305, USA. [2]Department of Physics, University of Colorado Boulder, Boulder, CO 80309, USA. [3]Department of Agronomy, Kansas State University, Manhattan, KS 66506, USA. [4]Department of Physics, Kansas State University, Manhattan, KS 66506, USA. [5]Time and Frequency Division, National Institute of Standards and Technology, Boulder, CO 80305, USA.
*Corresponding author. Email: daniel.herman@nist.gov

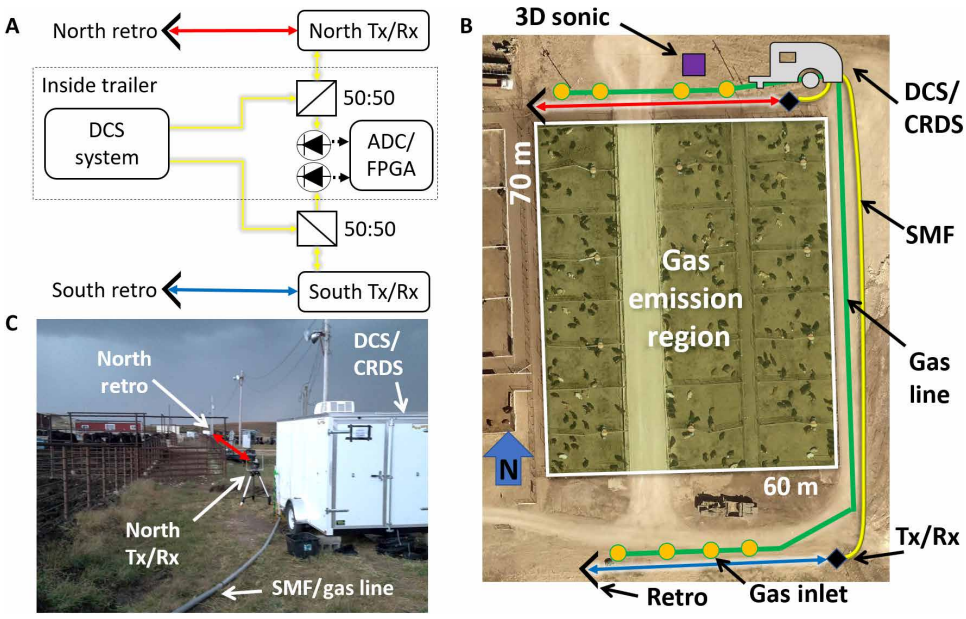

Fig. 1. Experimental setup. (**A**) Schematic of the dual-comb spectrometer for feedlot gas concentration measurements on two optical paths. Yellow lines indicate single-mode fiber (SMF) transmitting and receiving dual-comb light from the north (red arrow) and south (blue arrow) open-air paths. Note: Displayed 50:50 beam splitters were fiber based. ADC/FPGA, analog-to-digital converter and field-programmable gate array. (**B**) Aerial image of Manhattan, Kansas feedlot. Approximation location of the trailer (gray) containing DCS and CRDS systems is marked as well as that of the three-dimensional (3D) sonic anemometer (purple square), transmitting/receiving telescope (Tx/Rx; black diamonds), retroreflectors (black chevrons), gas inlets for the CRDS system (orange circles) and sampling gas line (green lines), north open-air path (red arrow), south open-air path (blue arrow), and SMF for dual-comb transport (yellow lines). The gas emission region only included the animal pens with an area of 3731 m^2. Photo credit: Riley County, Kansas. (**C**) Photograph of the north end of the site including the trailer housing both DCS and CRDS systems, the PVC tubing for south path SMF and gas line, Tx/Rx for the north path, and the north path retroreflector. Photo credit: Brian Washburn, NIST.

excess phase noise on the locks was subtracted in real time from the DCS interferogram signal using a field-programmable gate array (FPGA) (*20*, *21*). The repetition rate difference (rate of interferograms recorded per second) was set to 208 Hz. To tailor the comb spectrum, light for each comb was amplified to ~1 nJ per pulse in an erbium-doped fiber amplifier and sent through a short (~3 cm) piece of highly nonlinear fiber. The 35-THz wide spectra were filtered with 25-nm-wide band-stop fiber-coupled micro-optic filters centered near 1560 nm to block light without useful molecular absorption, maximizing achievable signal-to-noise ratio (SNR). The final DCS spectrum covered absorption features from CH_4, CO_2, NH_3, and H_2O (Fig. 2, A to D). For the DCS measurement, the filtered outputs were combined using a 50:50 fiber combiner generating two outputs that were directed over two open-air paths (Fig. 1A). Our DCS derives its concentration accuracy from high-resolution transmission molecular absorption database (HITRAN)–based (*22*, *23*) fitting routines and its wavelength accuracy from a Global Positioning System–disciplined quartz oscillator (*19*). There is no need for field calibration.

Measurement geometry

This work was performed at a Kansas State University beef cattle research unit outside of Manhattan, Kansas (Fig. 1, B and C). The 288 head of cattle at the site were contained in a pen measuring 70 m (north to south) by 60 m (east to west). Lasting from late October 2019 to early January 2020, the measurement captured gaseous emissions from both the cattle themselves (i.e., CH_4 from enteric fermentation) and area-distributed emissions (i.e., CH_4 and NH_3 from manure management). The DCS measured two paths, north and south of the cattle pen, allowing both an upwind measurement (background) and a downwind measurement (enhancement). In the Manhattan area, prevailing winds from autumn to winter are northerly and southerly (fig. S1A). Temperatures at the site varied widely from −10° to 20°C (fig. S1B). The site is surrounded by open, ungrazed pasture on all sides, providing stable background concentrations with values close to typical atmospheric background levels (*5*, *24*, *25*).

The DCS system was housed in a trailer parked on the feedlot's north side. A 10-m-long single-mode fiber (SMF) connected the first dual-comb output to the north telescope. The simple telescopes each consist of an ferrule connector/angled physical contact (FC/APC) fiber termination followed by a collimating 179-mm focal length, 102-mm diameter, and 45° off-axis parabolic mirror. About 10 mW of eye-safe collimated dual-comb light was directed at a 5-cm-diameter retroreflector positioned 50 m away, and the reflected signal was recoupled back into the launch fiber with about 25% efficiency. The returned dual-comb light was attenuated to ≤200 μW and coupled onto a 150-MHz bandwidth InGaAs photodiode. A significant advantage of near-infrared (NIR) DCS is the ability to use fiber to probe open-air paths far from the comb sources. To reach the south path, the dual-comb light was transported both ways through a 200-m-long duplexed SMF. Both telescopes were mounted on automatic gimbals that were realigned remotely using coaligned silicon charge-coupled device cameras. Each open-air path has slight height variations along its 50-m distance, ranging from 1.5 to 2.0 m above ground, which is included in the flux-estimation model described in Materials and Methods.

For each path, the InGaAs photodiode signal was low-pass filtered at 100 MHz and then digitized and phase-corrected in real time on an FPGA (*20*, *21*). In addition to these two DCS signals, inputs to the FPGA include the four phase-locked frequencies for

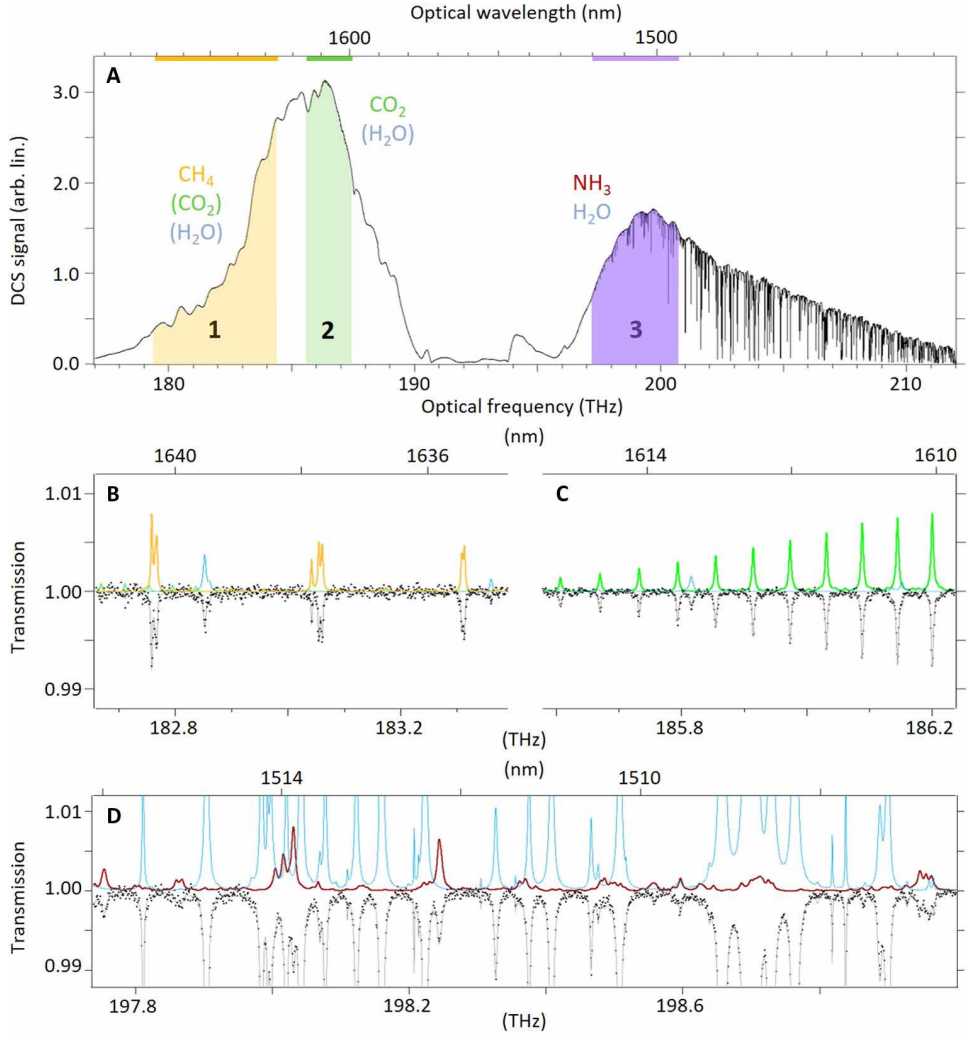

Fig. 2. Broadband, high-resolution DCS spectra taken at the downwind edge of the feedlot. (**A**) Full DCS spectrum at 5-min averaging time with highlighted sections showing the three spectral bands of interest (1, 2, and 3). Absorbing molecules are indicated each band with weak, interfering species shown in parentheses. (**B**) Example subsection of band 1. DCS data are shown in black with a fit to a HITRAN model in gray. The inverted axis shows transmission models for each individual species—CH_4 in yellow, H_2O in blue, CO_2 in green, and NH_3 in maroon. (**C**) Example subsection of band 2 with CO_2 and weak H_2O. (**D**) A subsection of band 3 highlighting the benefit of high resolution and large bandwidth, allowing retrieval of weak NH_3 in a strong interfering H_2O background. Note that, while DCS data in (B) to (D) are down-sampled to 1-GHz resolution for clear visualization, all fitting is done at the native resolution (200 MHz). Models shown here are for a 100-m round-trip path and 3.04 parts per million (ppm) CH_4, 452 ppm CO_2, 0.57% H_2O, and 1.23 ppm NH_3.

stabilizing the two combs (i.e., the two optical beat notes and two carrier-envelope offset frequencies), the two comb repetition rates, and an external 10-MHz clock. The real-time correction algorithm removes both phase and timing jitter in the interferograms and co-adds them to yield a single spectrum every 5 min. In addition, a three-dimensional sonic anemometer was positioned on a tower near the north path at approximately 3.5 m above the ground to record wind information every 100 ms.

RESULTS

DCS spectra and methane concentration retrievals

The DCS spectrum acquired at the feedlot over the standard 5-min integration time resolves hundreds of narrow absorption features over its 35-THz bandwidth, the broadest spectrum ever captured using atmospheric open-path DCS (Fig. 2A). The absorption from CH_4, CO_2, and H_2O below 190 THz is weak for these short 100-m round-trip optical path lengths, but one can observe the small percent-level absorption lines in zoomed-in spectra (Fig. 2, B and C). This small absorption provides enough signal to retrieve reliable concentrations with DCS. Above 198 THz, the water absorption becomes stronger and visible in the unexpanded spectrum. Underneath this strong water absorption are multiple weak NH_3 absorption features (Fig. 2D). Our ability to retrieve NH_3 concentrations amid this forest of strong water lines is evidence of the benefits of the bandwidth, resolution, and low spectral distortion possible with DCS. The total spectrum consists of over 175,000 spectral elements at 200-MHz point spacing (i.e., over 35 THz of optical bandwidth). The DCS figure-of-merit, defined as the product of the SNR and number of spectral elements, is in excess of 1.5×10^7 for a 5-min average, comparable to laboratory-based DCS systems (*12*).

Clear enhancements are visible in the time series of measured CH_4 concentrations from the DCS and CRDS systems for over 8 hours on the night of 17 November 2019 (Fig. 3A). Similar concentration time series are retrieved for NH_3 as discussed below and for H_2O and CO_2 as shown in the Supplementary Materials (fig. S2, A and B). CH_4 concentrations are averaged to 15-min time resolution, the minimum time over which our flux calculation is taken to be valid (*8*, *26*–*28*). Typically, CH_4 downwind enhancements with cattle present were 600 parts per billion (ppb) above the ~2 parts per million (ppm) background but could exceed 1 ppm during less windy periods. CH_4 concentrations from the two sensors and both paths compare well within the 25-ppb DCS experimental measurement precision estimated from the Allan-Werle deviations (*29*) of the upwind data (Fig. 3B). Allan-Werle deviations generalize the notion of measurement instability with each point signifying the measurement instability over a given averaging period. The CH_4 DCS precision at 900 s is 1.25 ppm·m (path-averaged concentration precision of 25 ppb), which matches the 1 to 3 ppm·m precision reported previously (*15*). Using the same method, the CRDS precision at 900 s was estimated to be ~2 ppb. An upward slope visible on the CRDS upwind Allan-Werle deviation (Fig. 3B) is driven by background CH_4 variability.

By this measure, the CRDS is an order of magnitude more precise than the DCS on the background (upwind) channel. However, this higher instrument precision ignores the added sampling uncertainty associated with intermittent point sensing compared to continuous open-path sensing. The strength of DCS is seen in the downwind channel, where DCS provides a more precise measure of gas concentration than CRDS (Fig. 3B) despite having higher instrument uncertainty. With only four gas inlets along each path and less than 50% uptime on either path for one 5-min measurement cycle, the CRDS is more susceptible to stochastic CH_4 plume variability than is the path-averaged and continuous dual-channel DCS sensor. In this experiment, the benefit in precision provided by continuous and path-averaged sampling is as large as 20 to 40 ppb (calculated as the difference in Allan-Werle deviations at 900 s for downwind DCS and CRDS), comparable to the background statistical precision of the DCS sensor of 25 ppb.

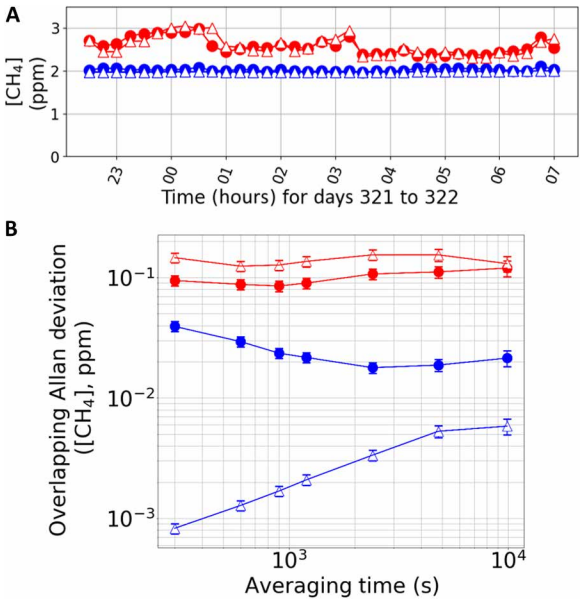

Fig. 3. Upwind and downwind CH_4 concentrations and associated instabilities. (**A**) Time series of DCS (closed circle) and CRDS (open triangles) measured north (red) and south (blue) dry concentrations of CH_4. (**B**) Allan-Werle analysis of CH_4 concentrations calculated using all data displayed in the above time series; upwind DCS (blue circles), downwind DCS (red circles), upwind CRDS (blue triangle), and downwind CRDS (red triangles). Note that the instability of the upwind concentrations is lower for the CRDS. For the downwind case, the DCS data show lower instability.

In this experiment, the homogeneous feedlot source provided a near ideal plume geometry for emissions quantification and yet the point sensor system still had decreased downwind precision due to insufficient temporal and spatial sampling. In a pasture system, where multiple, dispersed point sources create nonuniform plumes, a continuous integrated-path measurement will provide much larger improvements in precision over a multiport sampling system connected to a point sensor.

Methane flux

We examine an 11-hour period during the night of 24 November 2019 with appropriate weather conditions for flux retrievals with our IDM (see Materials and Methods) and complete coverage by both the DCS and CRDS systems (Fig. 4, A to E). The CH_4 concentrations are given for both the upwind and downwind paths from both the DCS and CRDS systems (Fig. 4B). In addition, the CH_4 flux from both the DCS and CRDS data is shown with the CH_4 flux from the feedlot showing clear time dependence on the hour time scale (Fig. 4, C and F). These changes are easily quantifiable with the 5-min resolution of our sensors and the averaged 15-min resolution of the flux calculation. The DCS and CRDS measurements yield similar time-dependent CH_4 fluxes from the feedlot with values ranging from 100 to 200 $\mu g/m^2$ per s. The CH_4 flux does show some disagreement during a period of small enhancement after 2:00 a.m. when winds were fast and near the edge of acceptable directions (Fig. 4C).

To compare the flux retrieved from the DCS and CRDS, we examine the correlation between values measured simultaneously with both sensors throughout the 4-month measurement campaign (Fig. 5). We fit a linear slope to this correlation by splitting the data into two groups: days with cattle present (day 305 to day 346) and days without cattle (day 347 to day 355). Even without cattle present, there is a baseline level of methanogenic bacterial activity in the feedlot manure, leading to CH_4 flux values with an average of 18 ± 11 $\mu g/m^2$ per s. The intercept of the linear regression of the days without cattle (i.e., small flux measurements) is used as the intercept for a linear fit to the entire flux dataset. The intercept is calculated to be 1.8 $\mu g/m^2$ per s (2% of typical CH_4 flux) and the slope is found to be 1.06, signifying a 6% bias between DCS and CRDS flux estimates. This close agreement between DCS and CRDS flux values was achieved without calibration of the DCS instrument as is required for continuous-wave (CW) laser sensors measuring comparable path-integrated concentrations (~100 ppm·m) (*30*). The demonstrated ability of DCS to measure CH_4 flux accurately without intensive calibration and on multiple remote fiber-connected paths enables wider deployment of DCS systems for CH_4 emissions inventory development and mitigation efforts.

Ammonia concentrations and flux

The same DCS instrument that allows for accurate, calibration-free quantification of feedlot CH_4 emissions simultaneously provides

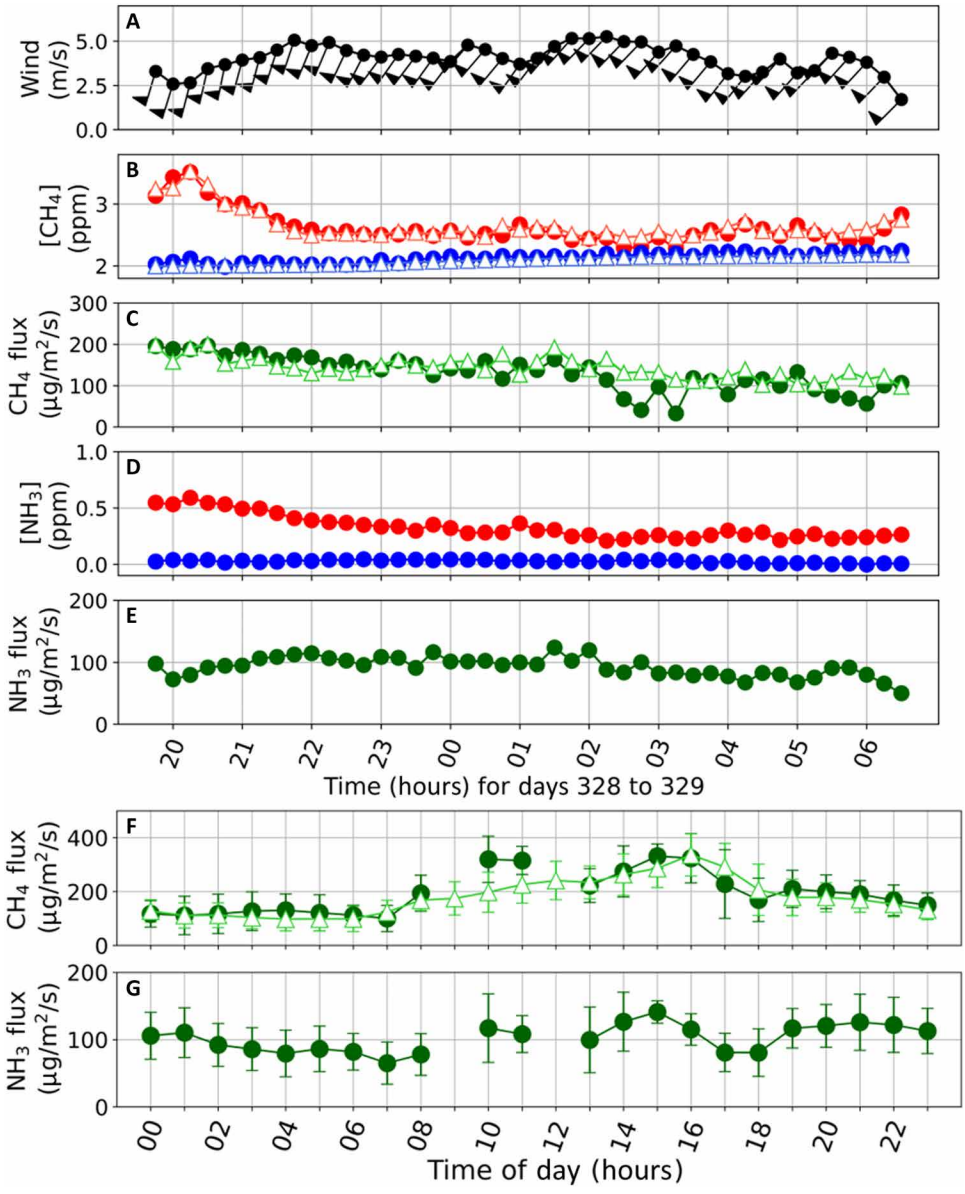

Fig. 4. Time-resolved CH_4 and NH_3 flux and averaged hourly diurnal flux cycles. Example dataset covering an 11-hour period showing (**A**) wind conditions at the measurement site, (**B**) CH_4 concentrations (averaged to 15-min time resolution) retrieved from the DCS (solid circles) and CRDS (open triangles) systems for north (red) and south (blue) paths, (**C**) the corresponding CH_4 flux retrieved from these DCS and CRDS measurements, (**D**) NH_3 concentrations from the DCS system, and (**E**) the corresponding NH_3 flux. The wind barbs point to the direction from which the wind is coming. (**F**) Diurnal cycle of CH_4 flux determined by DCS (solid circles) and CRDS (open triangles) when cattle were at the site (October 2019 to December 2019). Error bars are calculated by taking the SD of all 15-min averages included in each time bin. The increase in CH_4 flux between hours 8 and 16 is due to increased enteric fermentation after cattle feeding. (**G**) Diurnal cycle of NH_3 flux determined by DCS.

precise time-resolved NH_3 concentrations upwind and downwind of the feedlot (Fig. 4D). The average NH_3 background concentration was 60 ppb, equivalent to background feedlot NH_3 levels reported in the literature (*24*) but above standard atmospheric levels of 4 ppb (*25*). This elevated background is likely due to the proximity of the open-path sensors to the emission area. The average NH_3 enhancement was 430 ppb over background with some enhancements up to 1 ppm. An Allan-Werle deviation of the NH_3 background gives a precision of about ~10 ppb or 0.5 ppm·m at 900-s averaging time. The first demonstration of open-path DCS captured NH_3 absorption signatures with a beam passing over an open bottle of NH_3 (*31*). We return to these roots by demonstrating the first coherent, high resolution, open-path DCS detection of NH_3 that enables quantification of feedlot NH_3 flux with precision rivaling commercial sensors (*8*, *32*) while also providing vital CH_4 flux.

Using the same IDM as for CH_4, NH_3 fluxes were calculated at 15-min intervals (Fig. 4E). The fractional uncertainty in NH_3 flux measurement due to DCS instrument error alone is 3.5% for the average enhancement of 430 ppb (see Materials and Methods). The Allan-Werle deviation can also be applied directly to flux time series and results in a statistical precision at 900 s of 8 µg/m^2 per s (8% of average NH_3 flux). This analysis of instrument precision ignores

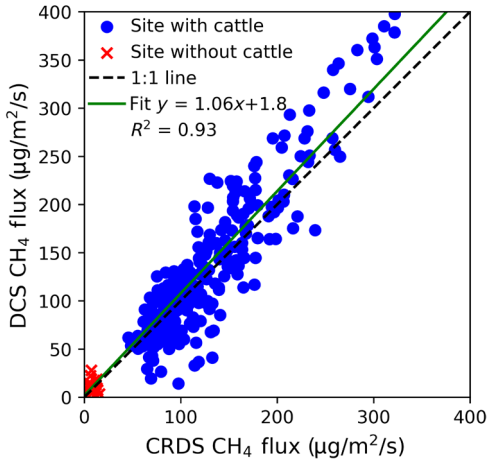

Fig. 5. Correlation between DCS and CRDS CH_4 flux. The data are fit to a line, determining the vertical intercept using fluxes without cattle (red x), and the slope was determined using all data. This process demonstrates 6% overall agreement between the DCS and CRDS CH_4 flux with a background offset of ~2 μg/m^2 per s (~2% of usual flux with cattle present).

potential biases from baseline distortion, detector nonlinearity, and cross-talk in the spectral model used to fit NH_3 and neighboring H_2O absorption features centered at 1510 nm (Fig. 2D). The uncertainty due to cross-talk is estimated at <5% (see the Supplementary Materials). Detector nonlinearity was not a large issue in this experiment as the received light was highly attenuated and no deep absorption lines were used in the analysis. The cepstral-domain fitting technique implemented in this work (see Materials and Methods) has been shown to be less sensitive to baseline fluctuations (*33*). Still, some bias in NH_3 concentration due to the choice of cepstral-domain filter function remains at a level comparable to the reported statistical precision (<5%). The combined uncertainty due to the effects discussed here is <10%, smaller than the ~20% disagreement found in previous comparisons of NH_3 flux estimation methods (*8*, *9*).

Diurnal cycles of methane and ammonia

The gas emission rate from the feedlot (and from agricultural systems in general) fluctuates over time, and thus, continuous measurement over a variety of conditions is necessary for complete understanding of these emission sources. Diurnal cycles for both CH_4 and NH_3 fluxes from the feedlot were generated by binning individual 15-min flux averages by hour of day for days when cattle were present (Fig. 4, F and G). In total, DCS data from 12 days are included in the diurnal cycle analysis, which amounted to 341 DCS flux calculations or an average of 14 DCS flux measurements per bin. A DCS flux average is only shown when the hour bin contains three or more 15-min averages (Fig. 4, F and G). The diurnal cycles with cattle present measured by DCS and CRDS match within statistical error bars. The morning hours are not as well covered by the DCS system as rapid temperature shifts and frosting on optical components made telescope alignment more challenging. Ruggedized telescopes developed for DCS oil and gas research will be incorporated in the future to mitigate this issue (*34*). The DCS itself operated robustly for the duration of the field campaign, breaking phase locks only a handful of times over the 3 months in the field.

A clear diurnal cycle in CH_4 production from the feedlot is observed with increased CH_4 fluxes during daylight hours (Fig. 4F). An increase in CH_4 appears after morning and afternoon feeding times (6 a.m. to 7 a.m. and 1 p.m. to 2 p.m.), suggesting that the source of the CH_4 emissions originates from increased cattle digestion and associated enteric fermentation (*4*, *35*). No such trend is seen in hourly binned data when the cattle were not present, although microbial activity in the manure still produces a small CH_4 flux. The nighttime CH_4 flux stabilizes as the cattle sleep, and the rate of enteric fermentation slows down considerably. The average DCS CH_4 flux during the presence of cattle (155 ± 85 μg/m^2 per s) minus the manure contribution (18 ± 11 μg/m^2 per s) gives an average cattle CH_4 flux of 137 ± 86 μg/m^2 per s. This number compares well with the Intergovernmental Panel on Climate Change (IPCC) 2006 (*18*) guideline number for beef cattle CH_4 emissions normalized to our feedlot size (~135 μg/m^2 per s), although every agricultural system is slightly different and deviations from this value are to be expected depending on cattle feed and manure management techniques.

For time periods with good data coverage (all times but 9 a.m. to 12 p.m.), the diurnal cycle for NH_3 (Fig. 4G) shows less variation than that of CH_4. The NH_3 diurnal cycle shows a more constant daily flux with an average of 104 ± 39 μg/m^2 per s or 116 g per head per day. This average compares well to literature values from measurements conducted in the central United States at concentrated dairy/beef cattle feeding operations during similar times of the year (*36*–*38*). For instance, the mean per capita emission rates of NH_3 during autumn months at two Texas panhandle beef cattle feedyards were 122 g per head per day and 83 g per head per day, measured using a single open-path CW laser sensor. The overall range of NH_3 emission rates from the same feedyards varied between 31 g per head per day in January and 207 g per head per day in October (*37*). All the NH_3 fluxes measured with cattle present at our Kansas test site fall within this range of values (Fig. 6A). NH_3 does not originate from digestive processes, rather it originates from hydrolysis of urea in the manure deposited on the ground in the feedlot pens and the emission rate fluctuates slightly over the course of the day, which has been observed in other feedlots as well (*39*). The lack of a clear pattern is attributed to the many factors that must be considered when studying the rate of hydrolysis of urea and subsequent volatilization of gaseous NH_3. It is known that temperature, soil water content, soil pH, and wind conditions can all modulate the rate of NH_3 release from agricultural soils (*40*). It is also known that differences in the variety of bacteria in soil can alter the dependences of any given soil ecosystem to the environmental factors (*41*).

Ammonia flux dependence on temperature and wind

Our open-path DCS measurement reveals the dependence of NH_3 flux on temperature and wind speed (Fig. 6). Assuming constant pH, soil temperature, total ammoniacal N in solution, and mass transport coefficient, the volatilization of NH_3 should generally follow a functional form proportional to Henry's volatility constant (K_h) for ammonia-water solution at a given temperature (*40*, *42*). This form can be expressed (*40*) as $K_h = (A/T)10^{6.123 - 1825/T}$, where A is a proportionality coefficient and T is the ambient air temperature in kelvin. A fit to this function is applied to the estimated NH_3 fluxes with an R^2 value of 0.36 (Fig. 6A), although it should be noted that a linear fit of the data provides a similar R^2 value. The fit conveys the general increase in volatilization as a function of ambient air temperature, which has been demonstrated previously (*43*, *44*). Factors such as microbial activity (*41*), manure pH (*40*), freeze-thaw cycles (*45*), and winds (*40*) contribute to large deviations from the Henry

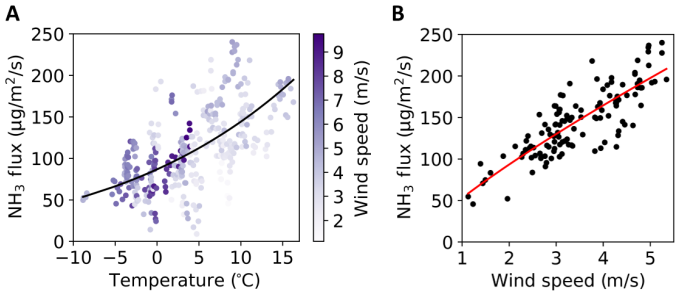

Fig. 6. Dependence of NH_3 emission rate on environmental parameters. (**A**) NH_3 flux (15-min averages) versus ambient air temperature. Color indicates 15-min averaged wind speed (*U*) for given flux estimate. Black line represents fit ($R^2 = 0.36$) to functional form for Henry's volatility constant (*40*). Note the large deviations of flux values near 0°C corresponding to complicated dynamics associated with freeze-thaw cycles. (**B**) NH_3 flux (15-min averages; black dots) versus *U* for ambient air temperature greater than 7°C. Red line represents fit ($R^2 = 0.65$) to power law $F = AU^B$ with $A = 56.1$ μg/m^2 per s and $B = 0.77$.

model. Microbial activity and manure pH were not measured but can reasonably be taken to vary on seasonal time scales (*43*). Evidence of complicated freeze-thaw dynamics is apparent in our single season dataset, with a large spread of reported flux estimates in the 0° to 5°C range, just above the freezing point of water. For fixed temperatures above the freezing point and fixed surface characteristic lengths, modeling shows (*40*) that volatilization scales nearly linearly with average wind speed, *U*. For temperatures above 7°C, a power law, $F = AU^B$,can be reliably fit ($R^2 = 0.65$) to the NH_3 flux data (Fig. 6B) yielding $B = 0.77$. This result falls very close to the literature value (*40*) of 0.8, good evidence of wind-dependent emission rates of NH_3 from the feedlot. The large dependence of NH_3 volatilization on environmental parameters stresses the importance of extended continuous field measurements such as those provided by calibration-free open-path DCS. For example, our results on the wind dependence of NH_3 emission rate will inform future studies aimed at reducing NH_3 emissions using modern management practices such as restricted grazing (*46*), targeted manure application (*47*), and agricultural windbreaks (*48*).

DISCUSSION

In this work, we demonstrate the advantages of broadband, high-resolution laser sensing by using coherent, open-path DCS for agricultural gas flux quantification for the first time at a small beef cattle feedlot. The large DCS bandwidth covered absorption from four different molecular species: CH_4, NH_3, CO_2, and H_2O. We specifically target the CH_4 and NH_3 emissions, which are the most important for this agricultural system. DCS simultaneously achieves sub-parts per million·meter detection sensitivity for NH_3 and parts per million·meter-level sensitivity for CH_4. Note that without the high resolution offered by our fully coherent technique, broadband sensing for NH_3 in this convenient band (located next to the useful telecom C-band) would be next to impossible due to H_2O clutter (Fig. 2D). Furthermore, the DCS is configured to measure across two displaced open-air paths using fiber-coupled telescopes. In this way, we continuously monitor the concentration over widely separated upwind and downwind open paths, which then allows for accurate flux estimation based on the directly observed concentration enhancement. We find the open-path configuration of the DCS captures downwind enhancements due to the gas emission with higher precision than a standard closed-path technique for certain wind conditions. When input to an IDM model, the upwind/downwind DCS data yield a CH_4 flux for the cattle feedlot that agrees to within 6% of the flux estimated by a co-located closed-path CRDS system, which is well within the 10% uncertainty attributed to flux models of this type (*28*). This agreement against a standard agricultural measurement technique gives us confidence that DCS accurately quantifies gas flux in an agricultural context. Because of the length of tubing required to transverse the feedlot site, a double path measurement of NH_3 using CRDS cannot easily provide a reliable benchmark. Yet, the retrieved NH_3 flux estimate from the DCS data generally agrees with the literature in terms of absolute magnitude and dependence on environmental parameters (Fig. 6).

A major motivation for this work is that the DCS system can be extended to estimate emissions from much larger areas. To this end, we briefly consider the requirements for estimating CH_4 flux from a 500 × 500 m pasture containing 40 cattle. When our values are scaled to 500-m paths, the achievable DCS precision at 900 s should be around 2 ppb, in line with previous NIR DCS demonstrations (*15*). Assuming a standard box model for the cattle emissions (*49*), we can scale the average CH_4 enhancement ($E = C_{sig} - C_{bkg}$) measured in our feedlot to a possible pasture enhancement (E') using the following relation

$$E' = E\frac{wN'}{w'N} \quad (1)$$

Note that *w* is the feedlot width (60 m), *w*′ is the pasture width (500 m), *N* is the number of cattle in the feedlot (288 head), and *N*′ is the number of cattle in the pasture (40 head). Equation 1 assumes that *w*′ is less than the average horizontal wind speed times the measurement integration period. This assumption should be satisfied for *w*′ = 500 m and a 15-min integration time. Using Eq. 1, the enhancement on the downwind edge of the 500 × 500 m would be, on average, around 10 ppb. By averaging fluxes, this enhancement will yield a CH_4 flux uncertainty of 10% after ~2.25 hours. For GHG inventories, one would like to measure weekly or monthly averaged emission with >10% flux uncertainty (*3*, *17*), which is easily supported at this time resolution. Subdividing the pasture with additional beam paths could greatly reduce averaging times if higher time resolution is required.

Looking toward the future, the open-path advantage of DCS motivates future pasture-scale flux estimation. As discussed above, the same approach used here should be applicable to CH_4 and NH_3 emissions from larger areas and will improve efforts to accurately quantify livestock and other agricultural contributions to GHG inventories. Open-path alternatives to standard techniques are especially advantageous for NH_3 detection given that the "sticky" and reactive nature of NH_3 demands difficult calibration of extractive NH_3 analyzers. Here, we have shown that DCS is a viable solution for sub–parts-per-billion level sensing of NH_3 over kilometer scales in a system that simultaneously provides information about multiple other gaseous species with precision comparable to single-species open-path sensors (*8*, *50*, *51*). The DCS NH_3 sensing has already provided useful in situ data regarding the wind dependence of NH_3 volatilization rates, simultaneously benchmarking biogeochemical models and encouraging further emissions mitigation research (*40*, *47*). In the future, multispecies DCS sensing will help determine accurate environmental dependences of CH_4-NH_3 and CO_2-NH_3 emission

factor ratios, ultimately improving our understanding of microbial activity and carbon exchange in feedlot and grassland ecosystems (*43*, *52*). While the current system operated in the NIR, continued advances of DCS further into the mid-IR provides opportunities for the flux quantification of a greater number of gasses and with greater sensitivity. In particular, the 2.0- to 2.4-μm spectral band presents increased sensitivity to CO_2, CH_4, and NH_3 and is accessed using photonic waveguides (*53*, *54*). In addition, many groups have recently demonstrated advances in mid-IR DCS sensing (*55*–*61*). The functional group region (3 to 5 μm) includes atmospheric transmission windows with access to strong CH_4, CO_2, and N_2O absorption. Precision N_2O emissions measurements are particularly interesting for the atmospheric sensing community as N_2O remains an understudied portion of global agricultural GHG emissions and a threat to the stratospheric O_3 layer (*62*). Field-scale DCS flux measurements covering multiple nitrogen-containing species (i.e., NH_3 and N_2O) will enable improved benchmarking of soil biogeochemical models (*63*). The mid-IR can also be used for sensing of biogenic volatile organic compounds and O_3, enabling advanced monitoring of plant health and agricultural aerosol production (*64*). As part of the larger vision of "precision agriculture," the frequency comb offers precise gas fluxes for many species simultaneously over large spatial scales, which will one day enable sustainable and more productive farming.

MATERIALS AND METHODS

CRDS setup

The DCS approach was also validated against a more traditional CRDS measurement of CH_4, CO_2, and H_2O performed using a commercial trace gas analyzer (G2311-f, Picarro), which was housed in the same trailer as the DCS system. Before the field deployment, the CRDS analyzer underwent a multipoint calibration using primary CH_4 and CO_2 World Meteorological Organization calibration standards (Global Monitoring Laboratory, NOAA, Boulder). At the measurement site, the CRDS analyzer was connected to a custom-built gas manifold. Four air inlets were deployed at the north edge of the feedlot, and another four air intakes were set up at the south edge of the feedlot. Each air intake consisted of a 1-m stainless steel tube (0.43-cm inner diameter) with a rain diverter and mesh screen in one of its extremities. The other extremity of the tube was connected to a stainless steel filter (7-μm sintered element filter). To prevent condensation, the filter holder was heated using a 0.5-W heater connected to a 12-V DC power supply, and a critical flow orifice located downstream of the filter was used to reduce the air pressure in the intake line and to ensure similar flow rate at all intakes. A polyethylene/aluminum tube (0.43-cm inner diameter) draws air from the intakes to the custom-made manifold.

The manifold was used to control the air flow from air intakes to the CRDS gas analyzer. The manifold switched between north and south air intakes every 30 s. The air was drawn continuously through all air intakes at a flow rate of approximately 1900 $cm^3\ min^{-1}$ using a diaphragm vacuum pump. A sample of the total flow was directed to the CRDS analyzer at a flow rate of 300 $cm^3\ min^{-1}$. All gas transported to the CRDS sample cell is heated to 60°C before measurement, and the CRDS only reports concentrations when its cell temperature is stable. Certified calibration tanks were used to verify the CRDS measurements every 6 hours. Concentrations measured by the CRDS gas analyzer were recorded at a rate of 10 Hz, and north and south paths data were averaged every 30 s. The first 15 s of data after switching intakes is discarded to ensure that the flushing of the sampling line is not included in the averaged measurement period.

Micrometeorological techniques and flux modeling

Gas emission flux is determined using an IDM (*27*) using the measured upwind and downwind concentrations combined with appropriate wind statistics as inputs. IDM is a well-established micrometeorological method to determine scalar exchange from well-defined source areas. This model is particularly adept at quantifying gas emissions from source areas with well-defined boundaries. The IDM uses the rise of concentration downwind from the source and wind statistics to determine the source emission rate. Numerous validation studies have been conducted under field conditions by releasing a tracer gas at a known flow rate and estimating the recovery rate with the IDM (*27*, *28*, *65*–*67*). These studies have reported an emission rate accuracy of ±10%. A freely available IDM software, WindTrax (*27*), was used for these dispersion simulations.

The IDM approach requires appropriate weather conditions to calculate reliable gas flux results, and data were filtered based on the following criteria. As WindTrax is only valid on 15-min or longer time scales, we averaged the 5-min raw concentration data to 15 min (900 s) (*8*, *27*). For our beam layout, wind direction (θ) was required to be northerly or southerly ($315° < \theta < 45°$ or $135° < \theta < 225°$). Acceptance criteria for friction velocity (u^*) and Monin-Obukhov Length (L) were set at $u^* > 0.1$ m/s and $|L| > 10$ m/s (*68*). The weather statistics at the site satisfied these criteria 60% of the total measurement time. The site wind conditions, temperature, and precipitation records are available for all measurements (fig. S1). The gas emission region (Fig. 2B) used by the IDM included only the cattle pens consisting of an area of 3731 m^2 (the road in between the pens was not included in the emission region). In WindTrax, both the DCS and CRDS north/south path concentration measurements were modeled as line concentration sensors with 30 points, starting at the telescope and ending at the retroreflector.

One of the principal sources of uncertainty in the IDM arises from the uncertainty in the concentration measurements themselves, either from the DCS instrument or CRDS instrument. The resulting fractional uncertainty in the flux can be estimated from the following

$$\frac{\sigma_F}{F} \sim \frac{\sqrt{2}\,\sigma_{C,\mathrm{bkg}}}{C_{\mathrm{sig}} - C_{\mathrm{bkg}}} \tag{2}$$

where F is the flux, σ_F is flux uncertainty, $\sigma_{C,\mathrm{bkg}}$ is the background concentration uncertainty, C_{sig} is the signal (downwind) concentration, and C_{bkg} is the background (upwind) concentration. This formula assumes equal precision on background and signal paths and ignores errors due to measurement deadtime and geometry as well as uncertainty in wind field measurements and inherent model uncertainty. Equation 2 is designed to capture the instrument contribution to measurement uncertainty. The average CH_4 enhancement (absolute value of the concentration difference between paths) measured by the CRDS and DCS over the course of the measurement campaign was approximately 600 ppb. Combining this average enhancement with our DCS precision of 25 ppb yields an average normalized DCS flux uncertainty of 6% using Eq. 2. For further comparison of CH_4 concentration measurements using DCS and CRDS, see the Supplementary Materials (fig. S3).

Concentration retrieval using cepstral analysis

The spectra are analyzed using a fit model derived from a combination of the HITRAN 2008 and 2016 databases and the cepstral-domain technique (*22*, *23*, *33*). HITRAN 2008 was used for all molecules except NH_3 for comparison with previous NIR DCS results. The dual-comb spectra are chopped into three bands: 1, 2, and 3, respectively, covering 179.3 to 184.3 THz, 197.2 to 200.7 THz, and 185.7 to 187.4 THz. These bands are used to retrieve CH_4, CO_2, and NH_3/H_2O, respectively (Fig. 2A). Temperature and pressure data for the fit model are provided by a sonic anemometer (*69*, *70*) and a weather station, respectively, which were both located on the same tower during the measurement campaign (Fig. 2B). The bias associated with fixing the temperature to this external value has a statistically negligible effect on CH_4 and NH_3 emission rates (see the Supplementary Materials). Band 1 contains CH_4, as well as weak carbon dioxide and water absorption features that are fixed by the fits from bands 2 and 3, respectively. The CH_4 model (HITRAN 2008) contains 108 features with line strength (S) > 10^{-22} cm^{-1}/(molecule × cm^{-2}). A cepstral-domain filter (lifter) (*33*) that mimics a high-pass filter in the frequency domain removes comb baseline structure broader than ~100 GHz for band 1. Band 2 contains both CO_2 and weak H_2O absorption. Thirty-six CO_2 features from HITRAN 2008 with $S > 10^{-24}$ cm^{-1}/(molecule × cm^{-2}) are included in the fit model. The H_2O concentration is held fixed at its value retrieved from band 3. A 40-GHz cepstral filter is used for band 2. Band 3 is fit to retrieve both H_2O and NH_3 concentrations. Fits in band 3 must deal with a large amount of spectral interference between species (Fig. 2D). In all, 82 H_2O features with $S > 10^{-24}$ cm^{-1}/(molecule × cm^{-2}) and 39 NH_3 features with $S > 10^{-21}$ cm^{-1}/(molecule × cm^{-2}) are included in the model for band 3. A 70-GHz cepstral filter is used for band 3. The filters are chosen by examining the structure of the cepstral fit residuals and are held constant for all analyses. Etalons are easily filtered out in the cepstral domain by adding notches to the cepstral filters to remove data points near the etalon appearance time (*33*). Strong H_2O absorption and overlapping weak CO_2 absorption are also measured below 1490 nm but are not analyzed in this work due to challenges associated with fitting deep absorption features. All reported DCS and CRDS concentrations are the dry values with the water concentration fixed to the value from each respective sensor.

SUPPLEMENTARY MATERIALS

Supplementary material for this article is available at http://advances.sciencemag.org/cgi/content/full/7/14/eabe9765/DC1

View/request a protocol for this paper from *Bio-protocol*.

REFERENCES AND NOTES

1. U.S. Environmental Protection Agency, Inventory of U.S. Greenhouse Gas Emissions and Sinks: 1990–2018. *EPA430-R-20-002* (2020); www.epa.gov/ghgemissions/inventory-us-greenhouse-gas-emissions-and-sinks-1990-2018.
2. A. Mosier, D. Schimel, D. Valentine, K. Bronson, W. Parton, Methane and nitrous oxide fluxes in native, fertilized and cultivated grasslands. *Nature* **350**, 330–332 (1991).
3. U.S. Environmental Protection Agency, Annexes to the Inventory of U.S. GHG Emissions and Sinks 1990–2018 (2020); www.epa.gov/ghgemissions/inventory-us-greenhouse-gas-emissions-and-sinks-1990-2018.
4. R. Todd, C. Moffet, J. Neel, K. Turner, J. Steiner, A. Cole, Enteric methane emissions of beef cows grazing tallgrass prairie pasture on the Southern Great Plains. *Trans. ASABE* **62**, 1455–1465 (2019).
5. T. K. Flesch, J. A. Basarab, V. S. Baron, J. D. Wilson, N. Hu, N. W. Tomkins, A. J. Ohama, Methane emissions from cattle grazing under diverse conditions: An examination of field configurations appropriate for line-averaging sensors. *Agric. For. Meteorol.* **258**, 8–17 (2018).
6. S. E. Bauer, K. Tsigaridis, R. Miller, Significant atmospheric aerosol pollution caused by world food cultivation. *Geophys. Res. Lett.* **43**, 5394–5400 (2016).
7. D. J. Miller, K. Sun, L. Tao, M. A. Khan, M. A. Zondlo, Open-path, quantum cascade-laser-based sensor for high-resolution atmospheric ammonia measurements. *Atmos. Meas. Tech.* **7**, 81–93 (2014).
8. H. Baldé, A. VanderZaag, W. Smith, R. L. Desjardins, ammonia emissions measured using two different GasFinder open-path lasers. *Atmospheres* **10**, 261 (2019).
9. K. von Bobrutzki, C. F. Braban, D. Famulari, S. K. Jones, T. Blackall, T. E. L. Smith, M. Blom, H. Coe, M. Gallagher, M. Ghalaieny, M. R. McGillen, C. J. Percival, J. D. Whitehead, R. Ellis, J. Murphy, A. Mohacsi, A. Pogany, H. Junninen, S. Rantanen, M. A. Sutton, E. Nemitz, Field inter-comparison of eleven atmospheric ammonia measurement techniques. *Atmos. Meas. Tech.* **3**, 91–112 (2010).
10. E. M. Waxman, K. C. Cossel, F. Giorgetta, G.-W. Truong, W. C. Swann, I. Coddington, N. R. Newbury, Estimating vehicle carbon dioxide emissions from Boulder, Colorado, using horizontal path-integrated column measurements. *Atmos. Chem. Phys.* **19**, 4177–4192 (2019).
11. S. Coburn, C. B. Alden, R. Wright, K. Cossel, E. Baumann, G.-W. Truong, F. Giorgetta, C. Sweeney, N. R. Newbury, K. Prasad, I. Coddington, G. B. Rieker, Regional trace-gas source attribution using a field-deployed dual frequency comb spectrometer. *Optica.* **5**, 320–327 (2018).
12. I. Coddington, N. Newbury, W. Swann, Dual-comb spectroscopy. *Optica.* **3**, 414–426 (2016).
13. N. Picqué, T. W. Hänsch, Frequency comb spectroscopy. *Nat. Photonics* **13**, 146–157 (2019).
14. G. B. Rieker, F. R. Giorgetta, W. C. Swann, J. Kofler, A. M. Zolot, L. C. Sinclair, E. Baumann, C. Cromer, G. Petron, C. Sweeney, P. P. Tans, I. Coddington, N. R. Newbury, Frequency-comb-based remote sensing of greenhouse gases over kilometer air paths. *Optica.* **1**, 290–298 (2014).
15. E. M. Waxman, K. C. Cossel, G.-W. Truong, F. R. Giorgetta, W. C. Swann, S. Coburn, R. J. Wright, G. B. Rieker, I. Coddington, N. R. Newbury, Intercomparison of open-path trace gas measurements with two dual-frequency-comb spectrometers. *Atmos. Meas. Tech.* **10**, 3295–3311 (2017).
16. J. Mangino, K. Peterson, H. Jacobs, in *12th International Emission Inventory Conference - "Emission Inventories - Applying New Technologies"* (San Diego, California, USA, 2003); www3.epa.gov/ttn/chief/conference/ei12/green/mangino.pdf.
17. Committee on Anthropogenic Methane Emissions in the United States: Improving Measurement, Monitoring, Presentation of Results, and Development of Inventories, Board on Atmospheric Sciences and Climate, Board on Agriculture and Natural Resources, Board on Earth Sciences and Resources, Board on Energy and Environmental Systems, Board on Environmental Studies and Toxicology, Division on Earth and Life Studies, National Academies of Sciences, Engineering, and Medicine, *Improving Characterization of Anthropogenic Methane Emissions in the United States* (National Academies Press, 2018); www.nap.edu/catalog/24987.
18. In *2006 IPCC Guidelines for National Greenhouse Gas Inventories* (Institute for Global Environmental Strategies, 2006), vol. 4; www.ipcc-nggip.iges.or.jp/public/2006gl/index.html.
19. G.-W. Truong, E. M. Waxman, K. C. Cossel, E. Baumann, A. Klose, F. R. Giorgetta, W. C. Swann, N. R. Newbury, I. Coddington, Accurate frequency referencing for fieldable dual-comb spectroscopy. *Opt. Express* **24**, 30495–30504 (2016).
20. J.-D. Deschênes, P. Giaccarri, J. Genest, Optical referencing technique with CW lasers as intermediate oscillators for continuous full delay range frequency comb interferometry. *Opt. Express* **18**, 23358–23370 (2010).
21. J. Roy, J.-D. Deschênes, S. Potvin, J. Genest, Continuous real-time correction and averaging for frequency comb interferometry. *Opt. Express* **20**, 21932–21939 (2012).
22. I. E. Gordon, L. S. Rothman, C. Hill, R. V. Kochanov, Y. Tan, P. F. Bernath, M. Birk, V. Boudon, A. Campargue, K. V. Chance, B. J. Drouin, J.-M. Flaud, R. R. Gamache, J. T. Hodges, D. Jacquemart, V. I. Perevalov, A. Perrin, K. P. Shine, M.-A. H. Smith, J. Tennyson, G. C. Toon, H. Tran, V. G. Tyuterev, A. Barbe, A. G. Császár, V. M. Devi, T. Furtenbacher, J. J. Harrison, J.-M. Hartmann, A. Jolly, T. J. Johnson, T. Karman, I. Kleiner, A. A. Kyuberis, J. Loos, O. M. Lyulin, S. T. Massie, S. N. Mikhailenko, N. Moazzen-Ahmadi, H. S. P. Müller, O. V. Naumenko, A. V. Nikitin, O. L. Polyansky, M. Rey, M. Rotger, S. W. Sharpe, K. Sung, E. Starikova, S. A. Tashkun, J. V. Auwera, G. Wagner, J. Wilzewski, P. Wcisło, S. Yu, E. J. Zak, The HITRAN2016 molecular spectroscopic database. *J. Quant. Spectrosc. Radiat. Transf.* **203**, 3–69 (2017).
23. L. S. Rothman, I. E. Gordon, A. Barbe, D. C. Benner, P. E. Bernath, M. Birk, V. Boudon, L. R. Brown, A. Campargue, J. P. Champion, K. Chance, L. H. Coudert, V. Dana, V. M. Devi, S. Fally, J. M. Flaud, R. R. Gamache, A. Goldman, D. Jacquemart, I. Kleiner, N. Lacome, W. J. Lafferty, J. Y. Mandin, S. T. Massie, S. N. Mikhailenko, C. E. Miller, N. Moazzen-Ahmadi, O. V. Naumenko, A. V. Nikitin, J. Orphal, V. I. Perevalov, A. Perrin, A. Predoi-Cross, C. P. Rinsland, M. Rotger, M. Simeckova, M. A. H. Smith, K. Sung, S. A. Tashkun, J. Tennyson, R. A. Toth, A. C. Vandaele, J. Vander Auwera, The HITRAN 2008 molecular spectroscopic database. *J. Quant. Spectrosc. Radiat. Transf.* **110**, 533–572 (2009).

24. S. M. McGinn, H. H. Janzen, T. W. Coates, K. A. Beauchemin, T. K. Flesch, Ammonia emission from a beef cattle feedlot and its local dry deposition and re-emission. *J. Environ. Qual.* **45**, 1178–1185 (2016).
25. "U.S. Standard Atmosphere, 1976" (U.S. Government Printing Office, Washington, D.C., 1976); https://ntrs.nasa.gov/search.jsp?R=19770009539.
26. H. F. Bonifacio, R. G. Maghirang, E. B. Razote, S. L. Trabue, J. H. Prueger, Comparison of AERMOD and WindTrax dispersion models in determining PM10emission rates from a beef cattle feedlot. *J. Air Waste Manage. Assoc.* **63**, 545–556 (2013).
27. T. Flesch, J. Wilson, L. Harper, B. Crenna, Estimating gas emissions from a farm with an inverse-dispersion technique. *Atmos. Environ.* **39**, 4863–4874 (2005).
28. T. K. Flesch, J. D. Wilson, L. A. Harper, B. P. Crenna, R. R. Sharpe, Deducing ground-to-air emissions from observed trace gas concentrations: A field trial. *J. Appl. Meteorol.* **43**, 487–502 (2004).
29. P. Werle, R. Mücke, F. Slemr, The limits of signal averaging in atmospheric trace-gas monitoring by tunable diode-laser absorption spectroscopy (TDLAS). *Appl. Phys. B Photophy. Laser Chem.* **57**, 131–139 (1993).
30. Z. J. DeBruyn, C. Wagner-Riddle, A. VanderZaag, Assessment of open-path spectrometer accuracy at low path-integrated methane concentrations. *Atmos.* **11**, 184 (2020).
31. A. Schliesser, M. Brehm, F. Keilmann, D. van der Weide, Frequency-comb infrared spectrometer for rapid, remote chemical sensing. *Opt. Express* **13**, 9029–9038 (2005).
32. E. D. Thoma, R. C. Shores, E. L. Thompson, D. B. Harris, S. A. Thorneloe, R. M. Varma, R. A. Hashmonay, M. T. Modrak, D. F. Natschke, H. A. Gamble, Open-path tunable diode laser absorption spectroscopy for acquisition of fugitive emission flux data. *J. Air Waste Manage. Assoc.* **55**, 658–668 (2005).
33. R. K. Cole, A. S. Makowiecki, N. Hoghooghi, G. B. Rieker, Baseline-free quantitative absorption spectroscopy based on cepstral analysis. *Opt. Express* **27**, 37920–37939 (2019).
34. C. B. Alden, S. C. Coburn, R. J. Wright, E. Baumann, K. Cossel, E. Perez, E. Hoenig, K. Prasad, I. Coddington, G. B. Rieker, Single-blind quantification of natural gas leaks from 1 km distance using frequency combs. *Environ. Sci. Technol.* **53**, 2908–2917 (2019).
35. P. Prajapati, E. A. Santos, Measurements of methane emissions from a beef cattle feedlot using the eddy covariance technique. *Agric. For. Meteorol.* **232**, 349–358 (2017).
36. W. F. Kissinger, R. K. Koelsch, G. E. Erickson, T. J. Klopfenstein, Characteristics of manure harvested from beef cattle feedlots. *Appl. Eng. Agric.* **23**, 357–365 (2007).
37. R. W. Todd, N. A. Cole, M. B. Rhoades, D. B. Parker, K. D. Casey, Daily, monthly, seasonal, and annual ammonia emissions from Southern High Plains cattle feedyards. *J. Environ. Qual.* **40**, 1090–1095 (2011).
38. D. L. Bjorneberg, A. B. Leytem, D. T. Westermann, P. R. Griffiths, L. Shao, M. J. Pollard, Measurement of atmospheric ammonia, methane, and nitrous oxide at a concentrated dairy production facility in southern idaho using open-path FTIR spectrometry. *Trans. ASABE* **52**, 1749–1756 (2009).
39. S. M. McGinn, T. K. Flesch, Ammonia and greenhouse gas emissions at beef cattle feedlots in Alberta Canada. *Agric. For. Meteorol.* **258**, 43–49 (2018).
40. F. Montes, C. A. Rotz, H. Chaoui, Process modeling of ammonia volatilization from ammonium solution and manure surfaces: A review with recommended models. *Trans. ASABE* **52**, 1707–1720 (2009).
41. J. D. Beuning, E. Pattey, G. Edwards, B. J. Van Heyst, Improved temporal resolution in process-based modelling of agricultural soil ammonia emissions. *Atmos. Environ.* **42**, 3253–3265 (2008).
42. N. J. Hutchings, S. G. Sommer, S. C. Jarvis, A model of ammonia volatilization from a grazing livestock farm. *Atmos. Environ.* **30**, 589–599 (1996).
43. S. J. Eilerman, J. Peischl, J. A. Neuman, T. B. Ryerson, K. C. Aikin, M. W. Holloway, M. A. Zondlo, L. M. Golston, D. Pan, C. Floerchinger, S. Herndon, Characterization of ammonia, methane, and nitrous oxide emissions from concentrated animal feeding operations in Northeastern Colorado. *Environ. Sci. Technol.* **50**, 10885–10893 (2016).
44. L. M. Golston, D. Pan, K. Sun, L. Tao, M. A. Zondlo, S. J. Eilerman, J. Peischl, J. A. Neuman, C. Floerchinger, Variability of ammonia and methane emissions from animal feeding operations in northeastern colorado. *Environ. Sci. Technol.* **54**, 11015–11024 (2020).
45. X.-F. Yu, Y.-X. Zhang, Y.-C. Zou, H.-M. Zhao, X.-G. Lu, G.-P. Wang, Adsorption and desorption of ammonium in wetland soils subject to freeze-thaw cycles. *Pedosphere* **21**, 251–258 (2011).
46. K. Voglmeier, M. Jocher, C. Häni, C. Ammann, Ammonia emission measurements of an intensively grazed pasture. *Biogeosciences* **15**, 4593–4608 (2018).
47. J. M. Pedersen, A. Feilberg, J. N. Kamp, S. Hafner, T. Nyord, Ammonia emission measurement with an online wind tunnel system for evaluation of manure application techniques. *Atmos. Environ.* **230**, 117562 (2020).
48. J. R. Brandle, L. Hodges, X. H. Zhou, in *New Vistas in Agroforestry: A Compendium for 1st World Congress of Agroforestry, 2004*, P. K. R. Nair, M. R. Rao, L. E. Buck, Eds. (Springer Netherlands, Dordrecht, 2004), *Advances in Agroforestry*, pp. 65–78; https://doi.org/10.1007/978-94-017-2424-1_5.
49. L. Ortolano, Estimating air quality impacts. *Environ. Impact Assess. Rev.* **5**, 9–35 (1985).
50. D. M. Bailey, E. M. Adkins, J. H. Miller, An open-path tunable diode laser absorption spectrometer for detection of carbon dioxide at the Bonanza Creek Long-Term Ecological Research Site near Fairbanks, Alaska. *Alaska Appl. Phys. B.* **123**, 245 (2017).
51. M. Nikodem, G. Plant, D. Sonnenfroh, G. Wysocki, Open-path sensor for atmospheric methane based on chirped laser dispersion spectroscopy. *Appl. Phys. B Lasers Opt.* **119**, 3–9 (2015).
52. C. E. Owensby, J. M. Ham, L. M. Auen, Fluxes of CO_2 from grazed and ungrazed tallgrass prairie. *Rangel. Ecol. Manag.* **59**, 111–127 (2006).
53. H. Guo, C. Herkommer, A. Billat, D. Grassani, C. Zhang, M. H. P. Pfeiffer, W. Weng, C.-S. Brès, T. J. Kippenberg, Mid-infrared frequency comb via coherent dispersive wave generation in silicon nitride nanophotonic waveguides. *Nat. Photonics* **12**, 330–335 (2018).
54. E. Baumann, E. V. Hoenig, E. F. Perez, G. M. Colacion, F. R. Giorgetta, K. C. Cossel, G. Ycas, D. R. Carlson, D. D. Hickstein, K. Srinivasan, S. B. Papp, N. R. Newbury, I. Coddington, Dual-comb spectroscopy with tailored spectral broadening in Si_3N_4 nanophotonics. *Opt. Express* **27**, 11869–11876 (2019).
55. G. Ycas, F. R. Giorgetta, E. Baumann, I. Coddington, D. Herman, S. A. Diddams, N. R. Newbury, High-coherence mid-infrared dual-comb spectroscopy spanning 2.6 to 5.2 μm. *Nat. Photonics* **12**, 202–208 (2018).
56. H. Timmers, A. Kowligy, A. Lind, F. C. Cruz, N. Nader, M. Silfies, G. Ycas, T. K. Allison, P. G. Schunemann, S. B. Papp, S. A. Diddams, Molecular fingerprinting with bright, broadband infrared frequency combs. *Optica.* **5**, 727–732 (2018).
57. M. A. Abbas, Q. Pan, J. Mandon, S. M. Cristescu, F. J. M. Harren, A. Khodabakhsh, Time-resolved mid-infrared dual-comb spectroscopy. *Sci. Rep.* **9**, 17247 (2019).
58. Z. Chen, T. W. Hänsch, N. Picqué, Mid-infrared feed-forward dual-comb spectroscopy. *Proc. Natl. Acad. Sci.* **116**, 3454–3459 (2019).
59. J. L. Klocke, M. Mangold, P. Allmendinger, A. Hugi, M. Geiser, P. Jouy, J. Faist, T. Kottke, Single-shot sub-microsecond mid-infrared spectroscopy on protein reactions with quantum cascade laser frequency combs. *Anal. Chem.* **90**, 10494–10500 (2018).
60. A. V. Muraviev, V. O. Smolski, Z. E. Loparo, K. L. Vodopyanov, Massively parallel sensing of trace molecules and their isotopologues with broadband subharmonic mid-infrared frequency combs. *Nat. Photonics* **12**, 209–214 (2018).
61. A. S. Kowligy, H. Timmers, A. J. Lind, U. Elu, F. C. Cruz, P. G. Schunemann, J. Biegert, S. A. Diddams, Infrared electric field sampled frequency comb spectroscopy. *Sci. Adv.* **5**, eaaw8794 (2019).
62. A. R. Ravishankara, J. S. Daniel, R. W. Portmann, Nitrous Oxide (N_2O): The dominant ozone-depleting substance emitted in the 21st century. *Science* **326**, 123–125 (2009).
63. K. Butterbach-Bahl, E. M. Baggs, M. Dannenmann, R. Kiese, S. Zechmeister-Boltenstern, Nitrous oxide emissions from soils: How well do we understand the processes and their controls? *Philos. Trans. R. Soc. B Biol. Sci.* **368**, 20130122 (2013).
64. S. Fares, D. R. Gentner, J.-H. Park, E. Ormeno, J. Karlik, A. H. Goldstein, Biogenic emissions from citrus species in California. *Atmos. Environ.* **45**, 4557–4568 (2011).
65. Z. Gao, R. L. Desjardins, T. K. Flesch, Assessment of the uncertainty of using an inverse-dispersion technique to measure methane emissions from animals in a barn and in a small pen. *Atmos. Environ.* **44**, 3128–3134 (2010).
66. Z. Loh, D. Chen, M. Bai, T. Naylor, D. Griffith, J. Hill, T. Denmead, S. McGinn, R. Edis, Measurement of greenhouse gas emissions from Australian feedlot beef production using open-path spectroscopy and atmospheric dispersion modelling. *Aust. J. Exp. Agric.* **48**, 244 (2008).
67. M. C. McBain, R. L. Desjardins, The evaluation of a backward Lagrangian stochastic (bLS) model to estimate greenhouse gas emissions from agricultural sources using a synthetic tracer source. *Agric. For. Meteorol.* **135**, 61–72 (2005).
68. R. W. Todd, M. B. Altman, N. A. Cole, H. M. Waldrip, methane emissions from a beef cattle feedyard during winter and summer on the Southern High Plains of Texas. *J. Environ. Qual.* **43**, 1125–1130 (2014).
69. S. P. Burns, T. W. Horst, L. Jacobsen, P. D. Blanken, R. K. Monson, Using sonic anemometer temperature to measure sensible heat flux in strong winds. *Atmos. Meas. Tech.* **5**, 2095–2111 (2012).
70. T. K. Flesch, V. S. Baron, J. D. Wilson, D. W. T. Griffith, J. A. Basarab, P. J. Carlson, Agricultural gas emissions during the spring thaw: Applying a new measurement technique. *Agric. For. Meteorol.* **221**, 111–121 (2016).

Acknowledgments: We would like to acknowledge initial constructive discussions with A. Chakrabarti, E. Minton, and K. Corwin. We would like to thank D. Blasi and W. Hollenbeck for granting access to the Kansas State University Beef Stocker Unit. We also thank J. Friedlein and N. Hoghooghi for useful comments on the manuscript. Use of manufacturers' or product names should not be construed as an endorsement. Contribution no. 21-222-J from the Kansas Agricultural Experiment Station. **Funding:** This work was partially funded by the NSF Division of Biological Infrastructure Award #1726304, the ARPA-E MONITOR program, the William and Joan Porter Endowment, the Habiger Heritage Fund, and NIST. **Author contributions:** D.I.H., N.R.N.,

S.M.W., B.D.D., I.C., E.A.S., and B.R.W. conceived of and designed the experiments. D.I.H., G.M.C., I.C., and B.R.W. built the DCS system. D.I.H., C.W., L.C.H., E.A.S., and B.R.W. performed the experiments. D.I.H., F.R.G., I.C., and B.R.W. analyzed the DCS data. C.W. and E.A.S. analyzed the CRDS data. B.R.W., E.A.S., D.I.H. and I.C. implemented the inverse dispersion model. B.R.W., D.I.H., I.C., E.A.S., K.C.C., and E.M.W. analyzed the flux data. D.I.H., B.R.W., I.C., and E.A.S. wrote the manuscript. B.R.W. and E.A.S. supervised the project. **Competing interests:** The authors declare that they have no competing interests. **Data and materials availability:** All data needed to evaluate the conclusions in the paper are present in the paper and/or the Supplementary Materials. Additional data related to this paper may be obtained from the authors upon a reasonable request.

Submitted 1 October 2020
Accepted 12 February 2021
Published 31 March 2021
10.1126/sciadv.abe9765

Citation: D. I. Herman, C. Weerasekara, L. C. Hutcherson, F. R. Giorgetta, K. C. Cossel, E. M. Waxman, G. M. Colacion, N. R. Newbury, S. M. Welch, B. D. DePaola, I. Coddington, E. A. Santos, B. R. Washburn, Precise multispecies agricultural gas flux determined using broadband open-path dual-comb spectroscopy. *Sci. Adv.* **7**, eabe9765 (2021).